A Novel Manipulator for 3D Ultrasound Guided Percutaneous Needle Insertion

H. Bassan, T. Hayes, R.V. Patel and M. Moallem

Abstract— The prostate is a small exocrine gland in men responsible for production of the liquid component of the seminal fluid. In North America, prostate cancer accounts for over 300,000 new cases and 40,000 deaths each year and it is the second leading cause of cancer death in men. Low-dose Rate (LDR) brachytherapy is gaining interest as a viable treatment option for prostate cancer due to its low side effects and high benefits. The present manual approach for brachytherapy needle insertion and the inherent flexibility of the needles make it extremely difficult to achieve accurate and consistent dosimetry. In this paper, we present a new 5 degrees-of-freedom (DOF) manipulator capable of performing percutaneous needle insertion. The manipulator can perform orientation, insertion and rotation of the needle and linear motion of the plunger to drop radioactive seeds at targeted locations. The manipulator is an integral part of a system utilizing a mechanically rotated side-fire transducer to create 3D ultrasound images of the organ and utilizing 3D SLICER software to visualize those images. Experiments conducted in agar phantoms reveal an average RMS targeting error of 1.45mm at an average insertion depth of 75.78mm proving the feasibility and efficacy of the proposed robotic system for percutaneous needle insertion.

Keywords: Prostate brachytherapy, percutaneous needle insertion, image-guided control

I. INTRODUCTION

The prostate is an important organ in male anatomy. A normal prostate measures about 40cm^3 in volume and has other organs in its immediate neighborhood such as the bladder and the rectum. In the later stages of life, two malignancies of prostate are commonly observed: Benign prostate hyperplasia (enlargement of the prostate) and prostate cancer.

Low-dose rate (LDR) brachytherapy is a minimally invasive form of therapy for prostate cancer. The procedure involves insertion of slender needles carrying radioactive seeds to perform therapy. In a typical procedure, somewhere between 15-20 needles carrying 80-100 seeds are utilized. In the present manual needle insertion approach, the needles are inserted through a rectilinear grid according to a preplanned dosimetry. The surgeon utilizes visual clues on a 2D ultrasound image to guide a needle tip towards a targeted location. Once the needle tip is at the target, the seeds are dropped by retracting the outer shell of the needle while keeping the plunger stationary. The accuracy and consistency of the procedure is highly dependent on the dexterity and experience of the surgeon. The inherent flexible nature of the needles also causes them to deflect during insertion, making needle insertion even more difficult. Multiple insertions are often required before the needle tip hits the target area, causing significant trauma to the patient and longer procedure times. Further, the horizontal template grid restricts the needle travel along parallel trajectories. This limitation prevents patients suffering from benign prostate hyperplasia from undergoing brachytherapy due to pubic arch interference.

Robotics-assisted percutaneous needle insertion has been proposed in recent years. A robotic approach to needle insertion can overcome some of the shortcomings of the manual approach. A robotic device can insert needles with consistent accuracy and it is possible to insert needles at oblique trajectories. Thus, patients deemed ineligible for brachytherapy due to pubic arch interference can be treated through the robotic insertion approach. Another advantage of a robotic system is that it can be integrated with an imaging modality to achieve an image-guided system, further enhancing the accuracy of the procedure. The system can also cut down procedure times by merging the pre-treatment dose planning and therapy in a single session. Some robotic systems for needle insertion have been reported in the literature. Robot-assisted approaches for percutaneous needle insertion guided by transrectal ultrasound (TRUS) and computed tomography (CT) are reported in [1] and [2] respectively. The robot consists of three independent stages for needle positioning, orientation and insertion. The mechanism however, does not include support for needle rotation or plunger motion. In [3], a manipulator capable of performing biopsies using TRUS is described, however only one DOF is motorized at present. Using an industrial manipulator and a manual needle insertion guide, a system for ultrasound guided biopsies has been reported in [4]. In [5], a mechanism for percutaneous needle insertion is described; however the system lacks the capability to perform oblique needle insertion. In [6], another mechanism is described for percutaneous needle insertion. The manipulator utilizes a planar mechanism with a second stationary link to achieve Remote Center of Motion (RCM). Needle insertion is performed manually and no provision is made for the plunger motion. Utilizing magnetic resonance imaging (MRI), a mechanism for needle insertion is described in [7]. The design utilizes planar drives similar

to that of [6] to create an RCM. The size of the manipulator is quite large and it is unsuitable for integration with an ultrasound system. Another manipulator using MRI guidance for percutaneous needle insertion is reported in [8]. In [9], transrectal access to the prostate is utilized to perform needle insertion. However, transrectal access can only be utilized for procedures involving a few needle insertions such as biopsies and hence this approach is somewhat limited for therapy. Another approach to percutaneous needle insertion based on a hand-held needle driver is described in [10]. It is however, difficult to keep such a device stationary for long periods of time without any support; thus precise needle placement will be difficult. In this paper, we present a new 5 DOF manipulator capable of performing percutaneous needle insertion under 3D ultrasound guidance. The manipulator can perform orientation, insertion and rotation of the needle and linear motion of the plunger to drop radioactive seeds at targeted locations. The manipulator is capable of achieving oblique needle insertion throughout the clinically relevant workspace to avoid pubic arch interference. Some of the key features of the manipulator are backdrivable joints, stationary actuators, redundant sensors and enhanced safety features.

II. KINEMATIC DESIGN

The kinematic structure of the manipulator is based on a two-tier design, often called a Macro-Micro system. The macro stage is responsible for the gross motions and is used to position the needle tip at the skin entry point. The micro stage carries out finer motions and performs the orientation and insertion of the needle. The macro-micro approach has been applied in the past to percutaneous procedures, e.g., in [6], [11]. This approach has benefits in terms of decoupled motions of the macro and micro stages, hence enhancing safety in the system. The process of needle insertion is carried out in steps: First utilizing the macro stage to bring the needle tip in contact with the skin entry point, and then utilizing the micro to orient the needle along the axis of insertion and finally, translating and rotating the needle until it reaches the target.

In order to determine joint motions and their ranges, discussions were conducted with surgeon's and actual procedures were carefully observed. It was decided that the micro manipulator should have a total of 5 DOF's: two for orientation, translation and rotation of needle along the axis of insertion and the plunger drive. Apart from having the desired degrees of freedom, the micro manipulator was required to have backdrivable joints, stationary actuators, redundant sensors and light-weight linkages. As a first prototype, the micro manipulator was required to be less than 5 Kg in weight and it was decided to machine it using aircraft grade aluminum. Further weight reduction is possible by manufacturing some parts of the manipulator from lighter materials such as Delrin. The micro manipulator was also required to have a force sensor to measure needle insertion forces.

Various kinematic designs were explored to find their suitability for micro manipulator. The orientation DOF's of the manipulator are required to meet an RCM kinematic constraint. Double parallelogram based Remote Center Kinematics were found to be most advantageous in terms of the number of required actuators, precision, simplicity of control and simpler design. Further, this design allowed for the RCM actuators to be located on the stationary part of the manipulator. Another advantage of this design is that it is possible to route transmission elements for the distal joints over the parallelogram linkages as accomplished in [12]. Initial kinematic simulation of the double-parallelogram structure revealed that there was very little clearance left from the patient to the robot linkages, hence this design was modified and a tool offset was introduced to avoid any collisions. Figure 1 shows the fully assembled micro manipulator.
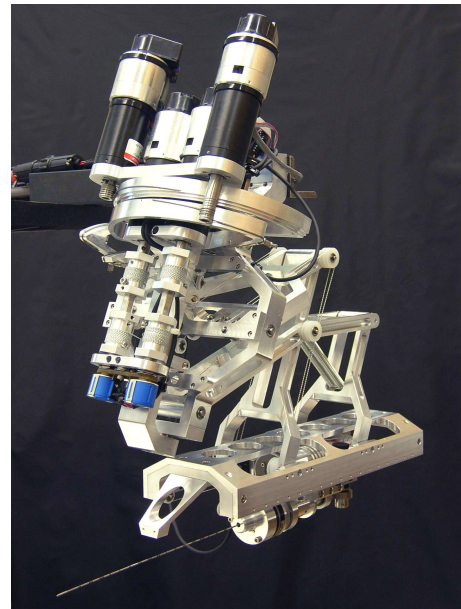

Fig. 1.   Micro manipulator.

In order to provide an extra safety feature in the manipulator, it was desirable to gravity balance the first two joints of the manipulator. Dynamic simulations were conducted with SimDesigner® to compute gravity balance torques for these two joints at various configurations and Matlab® was utilized to perform curve fitting to obtain closed-form equations for the gravity terms. For joint 1 (first RCM axis), a cubic polynomial approximated the gravity term with good accuracy and for joint 2 (second RCM axis), a 2-D fit was performed to approximate the gravity term. Joint 2 employs a partial spring balance to minimize the actuator torque required for gravity balancing. A linear spring with a spring constant of 0.729435 N/mm and free-length of 60mm provides partial compensation for the gravity term on this joint. These gravity terms were then experimentally verified on the manipulator and were found to give good results.

The translation and rotation of the needle about the axis of insertion are accomplished by a distal assembly, which is remotely actuated through the use of tendons. This allows

the actuators responsible for these motions to be located proximally on the stationary part of the manipulator. The tendons are routed over idler pulleys on the intermediate double-parallelogram links. Proximally, these tendons terminate on the motor wind up drums, and distally they terminate on the distal assembly of the manipulator. A key obstacle in designing a remote tendon actuation scheme is that the tendons have to maintain a constant length irrespective of any motions of the intermediate joints (RCM DOF's) of the manipulator. A novel tendon routing topology was invented for this manipulator which satisfies this constraint.

The distal assembly was designed to serve three purposes: provide needle attachment point on the manipulator, hold a (fifth) smaller motor for the plunger drive, and provide a wind up mechanism for the force sensor electrical cable. The fifth motor provides the plunger motion through the use of a rack and pinion transmission. The maximum travel length for the plunger motion was limited to 40 mm, based on the fact that each needle carries a maximum of 5 seeds with 5 spacers, each 4 mm in length. The distal assembly holds an off-the-shelf 6 DOF hollow force sensor (ATI industrial automation, Nano-43, SI-18-0.25). The needle is mounted on the manipulator such that the plunger passes through the center bore of the force sensor and the needle is attached to the tool flange of the force sensor. It has been hypothesized [5] that the rotation of the needle while it is being inserted can reduce needle tip deflection. To verify this, we have designed the manipulator such that it can provide the rotation of the needle. For a thorough description of the mechanical design of the manipulator, see [13].

The first four DOF's (two RCM, needle insertion and rotation) of the manipulator have redundant sensors (potentiometers) to enhance safety in the manipulator. The information from the potentiometers is merged with index information from the relative encoders on the motors to bring the manipulator to its home configuration (all joints at absolute zero joint angle). For simplicity, the first four actuators were chosen to be of the same type (Maxon RE35 with integrated brakes and HEDL5540 500 CPR encoders). For the results reported in this paper, a joint level PID controller with gravity balance was implemented on the manipulator. The dynamics of the manipulator are given by

$$\tau = M(\theta)\ddot{\theta} + V(\theta, \dot{\theta}) + G(\theta) \tag{1}$$

and the control law used is

$$\tau = K_p\, e + K_d\, \dot{e} + K_i \int e\, dt + G(\theta) \tag{2}$$

with

$$
\begin{aligned}
e &= \theta_d - \theta \\
\dot{e} &= \dot{\theta}_d - \dot{\theta}
\end{aligned}
\tag{3}
$$

where $M(\theta)$ is the manipulator mass matrix, $V(\theta, \dot{\theta})$ is the Centrifugal and Coriolis terms, e and $\dot{e}$ are the joint position

and velocity tracking errors, respectively. K_p, K_d and K_i are the proportional, derivative and integral gains respectively, and $G(\theta)$ is the gravity term.

A high-gain observer was preferred over ordinary differentiation to approximate joint velocities due to the lower resolution of the encoders. Let us denote the joint angle as θ and the respective joint velocity as ω, the estimated value of joint angle as $\hat{\theta}$ and the estimated joint velocity as $\hat{\omega}$. Then the discretized observer equations can be given as [14];

$$
\begin{aligned}
\hat{\theta}[kT] &= \frac{\epsilon\hat{\theta}[(k-1)T] + \epsilon T\hat{\omega}[(k-1)T] + \alpha_1 T\theta[kT]}{\epsilon + \alpha_1 T} \\
\hat{\omega}[kT] &= \hat{\omega}[(k-1)T] + \frac{\alpha_2 T}{\epsilon}(\theta[kT] - \hat{\theta}[kT])
\end{aligned}
\tag{4}
$$

where ϵ is a positive number, k is the sampling instant and T is the sampling period. Positive constants α_1 and α_2 are selected such that the roots of the equation

$$s^2 + \alpha_1 s + \alpha_2 = 0 \tag{5}$$

have negative real parts.

The control law was implemented on a Pentium IV, 1.6 GHz computer running the VxWorks® real-time operating system [15].

III. 3-D Ultrasound

The setup includes an Aloka SSD-1000 ultrasound system with a UST-672-5/7.5 bi-plane transrectal transducer. The video output from the ultrasound system is captured using a Matrox Meteor-II frame grabber card into a PC for further processing. The same PC also controls a custom designed rotator assembly which rotates the ultrasound probe about its central axis. The assembly includes a zero-backlash motor (Faulhaber 2232U024 motor with a 879:1 gearhead and a 512 CPR encoder) for actuation and a rotary potentiometer to provide absolute angle measurements. A standard PID control law with static friction compensation was implemented for the rotator assembly. Figure 2 shows the ultrasound rotator assembly.
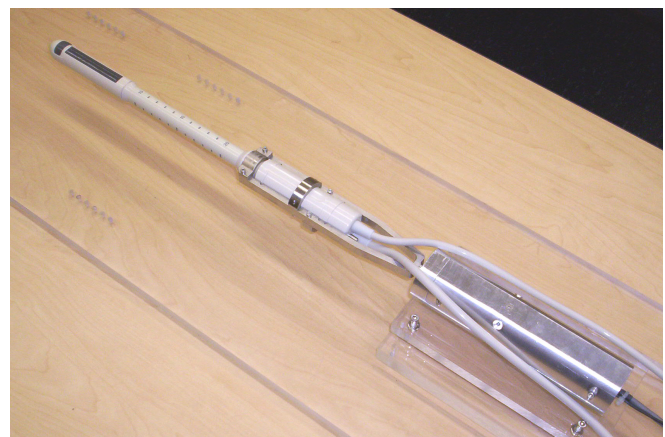

Fig. 2. Ultrasound rotator assembly.

In order to create 3D ultrasound images, a set of 100 2D B-mode ultrasound images are acquired at 0.7 degree intervals

as the probe is rotated about its axis by the rotator. In a clinical setup, for a typical prostate brachytherapy procedure these images will be separated by 1 degree intervals. These images appear as a fan (as shown in Figure 3) with its central axis aligned with that of the ultrasound probe. Figure 3 also shows the image coordinate system (z along the probe axis, y towards the top and x to the left). Before these images can be read into any visualization software, they are required to undergo a polar to rectangular transformation. The reconstruction algorithm computes new pixel values on a 3D Cartesian grid based on the pixel values from the input images acquired in the polar coordinate system. A destination-oriented method [16] is employed, where for each output pixel, the corresponding polar coordinates are computed. The pixel intensity from the nearest pixel in the polar coordinate image is then assigned to the output pixel.
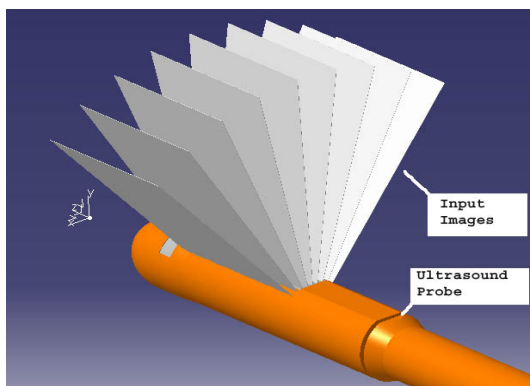

Fig. 3.   Graphical representation of input images.

For each z, let x, y be the coordinates of a point on the output Cartersian grid and r, θ the polar coordinates corresponding to that point. Then for nearest neighbor interpolation, first a nearest input image is found corresponding to θ and then the nearest pixel in that image is found corresponding to r. The pixel intensity of that pixel is assigned to the output pixel at x, y, z.

At present, it takes a few minutes for the reconstruction algorithm to compute a new set of Cartesian images (511x446x270, with a voxel size of 0.2x0.2x0.2 mm). Hence no real-time tracking of the needle is performed. Various techniques such as using a look-up table [16], are being investigated to achieve near real-time needle tracking and will be the subject of future experiments. Figure 4 shows the 3D SLICER user interface with a 3D scan of a prostate phantom. The upper window displays the 3D scan as three orthogonal intersecting planes. The same slices are also shown in three independent windows at the bottom of the user interface. The user can define a target point which is then indicated as a fiducial marker in 3D image.

IV. EXPERIMENTAL SETUP

Figures 5 and 6 show the system block diagram and experimental setup respectively. The system consists of an imaging computer to capture and visualize ultrasound images
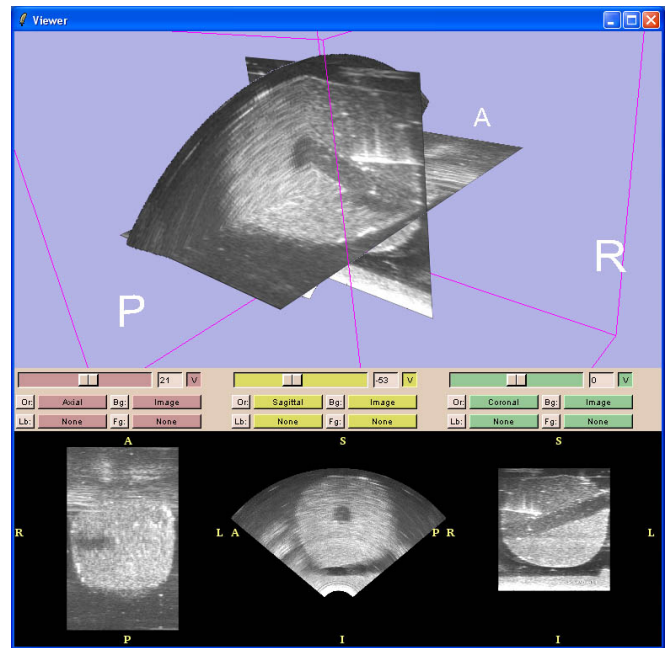

Fig. 4.   3D SLICER software interface.

and another computer to control the micro manipulator. The two computers are interfaced to each other through a TCP/IP connection over ethernet, However, at present the information flow is only from the imaging computer to the control computer.
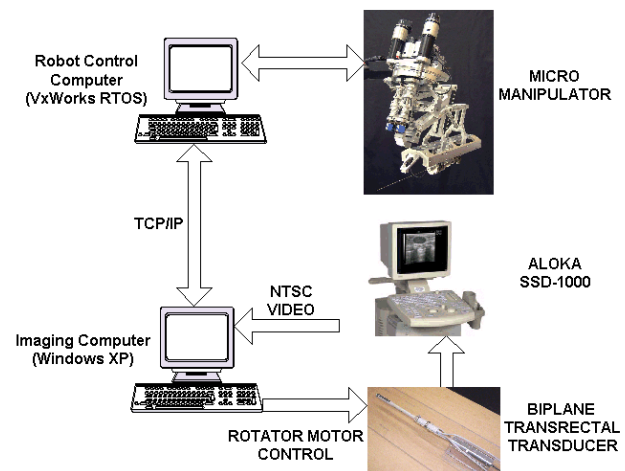
Fig. 5.   System block diagram.

The micro manipulator is mounted on a manually driven XYZ stages for the experiments reported in this paper. These stages have $1\mu m$ resolution and allow for functional testing of the micro manipulator. Later, the macro manipulator will be utilized to carry the micro manipulator and position it at the skin entry point.

A custom built container was utilized to make agar phantoms for the experiments. One wall of the container has a removable (100x100mm) window through which the needle

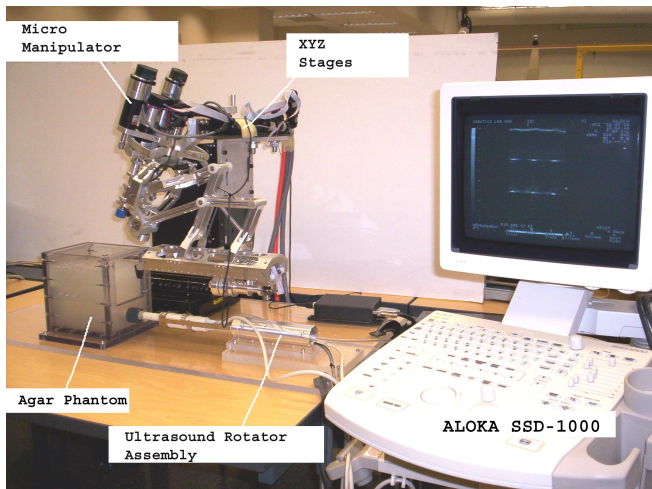Fig. 6. Experimental Setup.

is inserted. The container also includes a hole to simulate the rectum and accommodate the ultrasound probe. The same container was also utilized to calibrate the ultrasound system. Two opposite sides of this container were machined with rectangular grid holes (3x5 holes, 0.5mm diameter) separated by 30mm in the first direction and 20mm in the second direction. In order to calibrate the ultrasound system, 0.35mm diameter copper wires were stretched across these holes and then scanned in a water bath. Pixels/mm values for the ultrasound system were then computed by comparing the measured distances (in image coordinates) to the actual distances. Figure 7 shows a close-up view of the container. Both the robot and the ultrasound system were spatially registered to the container, thus the target point can be easily converted to the robot coordinate system.
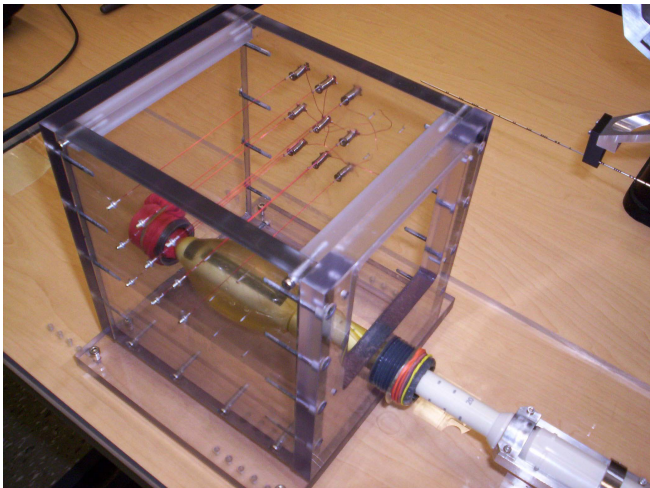

Fig. 7. Custom build container for ultrasound calibration and needle insertion experiments.

The steps involved in targeting a point are as follows:

1) A pre-scan is performed as the ultrasound probe is rotated ±35 degrees and images are acquired and saved onto the hard disk.

2) The reconstruction algorithm loads these images into memory and computes a new set of Cartesian images based on the nearest neighbor interpolation.

3) The user loads the reconstructed images into the 3D SLICER [17] software for visualization and defines a target point.

4) The coordinates of the target point are sent to the control computer through a TCP/IP connection.

5) The control software performs bound checking on the target point and executes the desired trajectory to bring the needle tip to the target point. The trajectory is executed in two steps; (a) The RCM stage orients the needle along the desired insertion path; (b) The distal stage translates and/or rotates the needle towards the target.

6) Another full scan and interpolation is performed and the data is loaded into 3D SLICER to verify the targeting accuracy.

7) Steps 3-6 are repeated for each of the remaining target points.

V. RESULTS

An 18G 20cm bevel-tip brachytherapy needle (Cook Urological, Spencer, Indiana) was mounted on the manipulator for the experiments. The phantom was created with a mixture (% weight): water (98.25%), and Gelrite Gellan Gum (1.75%) (Sigma-Aldrich, St. Louis, MO).

A total of 14 target points were selected at various insertion depths and angulation values for the experiment. The points were selected so as to cover the clinically relevant workspace to validate the applicability of the manipulator. Upward tilting trajectories were also performed to avoid pubic arch interference. For the first RCM axis, the angulation values varied from -22.7 to +17.89 degrees. For the second RCM axis, the angulation values covered a range from -10.37 to +12.65 degrees. The needle insertion depth varied from 47.7mm to 90.93mm. Table I shows the targeted point and respective targeting error.

TABLE I
TARGET POINTS AND RESPECTIVE ERROR.

Label	Insertion Depth (mm)	RMS error (mm)
P1	47.70	1.23
P2	51.19	0.56
P3	67.70	1.13
P4	68.58	0.97
P5	70.21	1.92
P6	71.77	2.04
P7	71.84	1.56
P8	71.84	1.28
P9	87.70	1.40
P10	89.00	0.56
P11	90.62	2.97
P12	90.93	1.34
P13	90.93	1.60
P14	90.93	1.75

In order to verify the needle insertion accuracy, a post-scan

was carried out after the needle reached the targeted depth. The reconstructed data was then loaded into 3D SLICER and the needle tip was manually segmented in three orthogonal slices (referred to as the axial, sagittal and coronal planes in 3D SLICER). The axial, sagittal and coronal planes were manually translated until satisfactory visualization of the needle was achieved. These three pixel coordinates were then assigned as the needle tip.

The pixel RMS error between the needle tip coordinates and the targeted point was computed and given by

$$e_p \;=\; \sqrt{S^2 + R^2 + A^2} \tag{6}$$

where S, R and A are the pixel errors in the axial, sagittal and coronal planes, respectively. The RMS error was then converted into millimeters by multiplying by 0.2 (voxel size).

The average RMS targeting error was found to be 1.45mm and the average insertion depth was 75.78mm. 85.7% of the needle insertions were within less than 2mm error.

VI. Discussion

Various sources of system errors were also briefly analyzed. It was found that the manipulator reached the target points in free air with good accuracy. Initial tests in air revealed less than 0.8mm RMS error on the angulation extremities of the manipulator at 120mm needle travel.

During the experiments, a small amount of needle deflection was also observed, but for the results reported in this paper, no needle correction was performed. The agar phantom used during the experiments was constructed as homogeneous (material poured in a single step and let set overnight) and therefore the needle deflection can be assumed to be uniform at various locations inside the phantom. It was also noted that even a slight angulation of the manipulator could lead to noticeable needle deflection during insertion. The deflection was found to increase as the insertion depth increased. The errors reported in Table I also include needle deflection errors.

Another difficulty observed during the experiments was the low resolution of ultrasound images, especially at deeper depth levels. Further, for oblique needle insertion, very little energy gets reflected back to the transducer and an artifact that appears to be an extension of the needle was observed in those cases. The combined effect made it difficult to pinpoint the needle tip in the ultrasound images. Although the quality of the image can be somewhat improved by incorporating a high-end ultrasound system, it is highly unlikely that the artifacts can be completely eliminated.

No force sensor readings were utilized in the experiments presented in this paper, but will be the subject of future experiments. It was also difficult to obtain multiple samples at each point due to air pockets introduced by previous needle insertion.

VII. Conclusion

A new robotic manipulator for percutaneous needle insertion was discussed in this paper. The mechanism has five active degrees-of-freedom: orientation (2 DOFs), translation and rotation of the needle and the plunger motion. A custom built rotator assembly was utilized to create 3D ultrasound images and the 3D SLICER software was used as the user interface to visualize and define target points in those images. Experimental results for needle insertion in agar phantoms revealed that 85.7% of the needle insertions had less than 2mm error. Future work will involve needle insertion experiments with tissue phantoms and implementation of a force control scheme to reduce needle tip deflection.

References

[1] G. Fichtinger, E. C. Burdette, A. Tanacs, A. Patriciu, D. Mazilu, L. L. Whitcomb, and D. Stoianovici, "Robotically assisted prostate brachytherapy with transrectal ultrasound guidanced–phantom experiments," in *Brachytherapy*, vol. 5, 2006.

[2] G. Fichtinger, T. L. DeWeese, A. Patriciu, A. Tanacs, D. Mazilu, J. A. Anderson, K. Masamune, R. H. Taylor, and D. Stoianovici, "System for robotically assisted prostate biopsy and therapy with intraoperative CT guidance," in *Journal of Academic Radiology*, vol. 9, 2002.

[3] L. Phee, D. Xaio, J. Yuen, C. F. Chan, H. Ho, C. H. Thng, C. Cheng, and W. S. Ng, "Ultrasound guided robotic system for transperineal biopsy of the prostate," in *Proc. IEEE Int. Conference on Robotics and Automation*, 2005.

[4] G. Megali, O. Tonet, C. Stefanini, M. Boccadoro, V. Papaspyropoulos, L. Angelini, and P. Dario, "A computer-assisted robotic ultrasound-guided biopsy system for video-assisted surgery," in *Proc. of the International Conference on Medical Image Computing and Computer-Assisted Interventions (MICCAI)*, 2001.

[5] B. L. Davies, S. J. Harris, and E. Dibble, "Brachytherapy-an example of a urological minimally invasive robotic procedure," in *Int. Journal of Medical Robotics and Computer Assisted Surgery*, vol. 1, 2004.

[6] G. Kronreif, M. Fürst, J. Kettenbach, M. Figl, and R. Hanel, "Robotic guidance for percutaneous interventions," in *Journal of Advanced Robotics*, vol. 17, 2003.

[7] K. Chinzei and K. Miller, "Towards MRI guided surgical manipulator," in *Int. Medical Journal for Experimental and Clinical Research*, vol. 7, 2001.

[8] S. DiMaio, G. Fischer, S. Haker, N. Hata, I. Iordachita, C. Tempany, R. Kikinis, and G. Fichtinger, "A system for mri-guided prostate interventions," in *Proc. Int. Conference on Biomedical Robotics and Biomechatronics*, 2006.

[9] C. M. Schneider, A. M. Okamura, and G. Fichtinger, "A robotic system for transrectal needle insertion into the prostate with integrated ultrasound," in *Proc. IEEE Int. Conference on Robotics and Automation*, vol. 1, 2004.

[10] S. Okazawa, R. Ebrahimi, J. Chuang, S. E. Salcudean, and R. Rohling, "Hand-held steerable needle device," in *IEEE Trans. on Mechatronics*, vol. 10, 2005.

[11] D. Stoianovici, K. Cleary, A. Patriciu, D. Mazilu, A. Stanimir, N. Craciunoiu, V. Watson, and L. Kavoussi, "Acubot: A robot for radiological interventions," in *IEEE Trans. on Robotics and Automation*, vol. 19, 2003.

[12] A. J. Madhani, G. Niemeyer, and J. K. S. Jr., "The Black Falcon: A teleoperated surgical instrument for minimally invasive surgery," in *Proc. IEEE Int. Conference on Intelligent Robots and Systems*, vol. 2, 1998.

[13] H. Bassan, R. V. Patel, and M. Moallem, "A novel manipulator for prostate brachytherapy: Design and preliminary results," in *Proc. of the 4th IFAC Symposium on Mechatronics Systems*, 2006.

[14] H. Khalil, "Adaptive output feedback control of nonlinear systems represented by input-output models," in *IEEE Transactions of Automatic Control*, vol. 41, 1996.

[15] *VxWorks Programmer's Guide*. 500 Wind River Way, Alameda, CA, USA 94501, 2004.

[16] S. Tong, D. B. Downey, H. N. Cardinal, and A. Fenster, "A three-dimensional ultrasound prostate imaging system," in *Ultrasound in Medicine and Biology*, vol. 22, 1996.

[17] www.slicer.org.